Title
The Effect of a Mainshock on the Size Distribution of the Aftershocks

Journal
Geophysical Research Letters, 45(24)

ISSN
0094-8276

Authors
Gulia, L
Rinaldi, AP
Tormann, T
et al.

Publication Date
2018-12-28

DOI
10.1029/2018gl080619

Peer reviewed

The Effect of a Mainshock on the Size Distribution of the Aftershocks

L. Gulia[1], A. P. Rinaldi[1], T. Tormann[1], G. Vannucci[2], B. Enescu[3], and S. Wiemer[1]

[1] Swiss Seismological Service, ETH, Zurich, Switzerland, [2] Istituto Nazionale di Geofisica e Vulcanologia, Bologna, Italy, [3] Department of Geophysics, Kyoto University, Kyoto, Japan

Correspondence to: L. Gulia, lgulia@ethz.ch

Abstract

A systematic decay of the aftershock rate over time is one of the most fundamental empirical laws in Earth science. However, the equally fundamental effect of a mainshock on the size distribution of subsequent earthquakes has still not been quantified today and is therefore not used in earthquake hazard assessment. We apply a stacking approach to well-recorded earthquake sequences to extract this effect. Immediately after a mainshock, the mean size distribution of events, or *b* value, increases by 20–30%, considerably decreasing the chance of subsequent larger events. This increase is strongest in the immediate vicinity of the mainshock, decreasing rapidly with distance but only gradually over time. We present a model that explains these observations as a consequence of the stress changes in the surrounding area caused by the mainshocks slip. Our results have substantial implications for how seismic risk during earthquake sequences is assessed.

Plain Language Summary

The effect of a mainshock on the size distribution of subsequent earthquakes has not been quantified and is therefore not used in earthquake hazard assessment. To quantify this effect, we develop a stacking approach centered on the mainshock time and apply it to for 31 well-recorded aftershock sequences from around the world. We found that after a mainshock the earthquake size distribution shifts toward relative more smaller events, increasing the so-called *b* value by 20–30%. One of the consequences of our finding is that the rates of large aftershocks are overestimated by the currently used models. Our result is fully consistent with both laboratory measurements and modeling, and we present a conceptual model that explains our findings.

1 Introduction

Earthquakes interact with each other by changing the state of stress in their surroundings (Stein, 1999). The static and dynamic stress changes caused by their instantaneous displacement decay with growing distance from the fault (Okada, 1992). The most noticeable consequence of this stress change is a dramatic increase in the seismicity rate (Ebel et al., 2000). The aftershock phenomenon is one of the most intensely studied properties of such events.

Based on empirical observations of the 1891 Nobi earthquake, Omori (1895) described how aftershock activity decreased by $K/(t + c)$, where K and c are constants that describe aftershock productivity and delay time (Utsu et al., 1995). Utsu (1961) defined the so-called modified Omori Formula, observing that aftershock sequences decay with different exponents. Alternatives to the Omori law have also been proposed (Mignan, 2015, 2016). Today, aftershock activity is typically described as part of a cascading or branching process, and the Epidemic-Type Aftershock Sequence (Ogata, 1988, 1998) Model is the best currently available statistical description of seismicity (Marzocchi et al., 2017). There is also a good physics-based understanding, often derived from laboratory friction experiments (Toda et al., 2005), of how stress changes cause the seismicity rate to increase in some regions by a factor of 1,000 or more, whereas, in other regions, Coulomb stress changes induced by a mainshock may be negative, lowering the earthquake rate (Gerstenberger et al., 2005; Wyss & Wiemer, 2000).

However, changes in stress should impact not only earthquake activity rate but also the frequency size, or frequency magnitude, distribution (FMD) of the subsequent earthquakes. The FMD is typically described using another fundamental empirical law of seismology, the “Gutenberg-Richter relationship” (Gutenberg & Richter, 1944), which estimates the number of earthquakes N larger than or equal to magnitude M, via the formula $\log(N) = a - bM$, whereby the a value is a volume productivity measure and the b value quantifies the FMD slope: a lower b value describes a distribution with a higher proportion of larger magnitudes, and vice versa. Repeated laboratory measurements (Amitrano, 2003; Goebel et al., 2013; Scholz, 1968) have established that the applied differential stress to a rock sample determines the b value: the higher the applied differential stress, the lower the b value. Observations from various tectonic contexts are consistent with this inverse proportionality of b on differential stress (Schorlemmer et al., 2005), indicating, for example, b values' systematic dependency on faulting style (Gulia & Wiemer, 2010), depth (Spada et al., 2013), and fluid pressure (Bachmann et al., 2012).

To date, the effect of a mainshock's differential stress change on the subsequent seismicity has not been systematically investigated, but individual case studies suggest that sometimes higher b values are observed after a mainshock (Ogata & Katsura, 2014; Tamaribuchi et al., 2018; Tormann et al., 2012, 2014, 2015; Wiemer et al., 2002; Wiemer & Katsumata, 1999). These individual observations highlight the important question of whether such high postmainshock b values are characteristic of aftershock sequences and, if so, whether, when or how they recover. Here for the first time, we use a stacking approach to b value time series to enhance the signal-to-noise ratio of their changes, allowing us to extract the generic behavior previously masked by random variations and systematic biases.

2 Data and Method

Transients in *b* value are difficult to establish with confidence, since temporal variation can easily be mimicked or masked by spatial activation changes (Tormann et al., 2013; Wiemer et al., 2002), especially when the completeness of recording changes dramatically over time (Wiemer & Wyss, 2002). Consequently, any robust analysis of transients necessitates meticulous sequence-specific data selection systematically applied so as not to introduce any biases into the analysis.

We defined a fast, homogeneous, objective, and reproducible methodology to select the region for analysis based on the mainshock's focal mechanism (FM). FMs provide all required information (strike, dip, and rake) to model a first-order rectangular fault plane. By deriving a tectonic fault style (Frohlich, 1992) and by applying empirical formulas (Wells & Coppersmith, 1994), source dimensions and relative uncertainties can be derived directly from the mainshock magnitude (Figure 1). Between the two available nodal planes, we consider the one with the highest number of immediate aftershocks (hereinafter we refer to the chosen fault plane as the *box*).

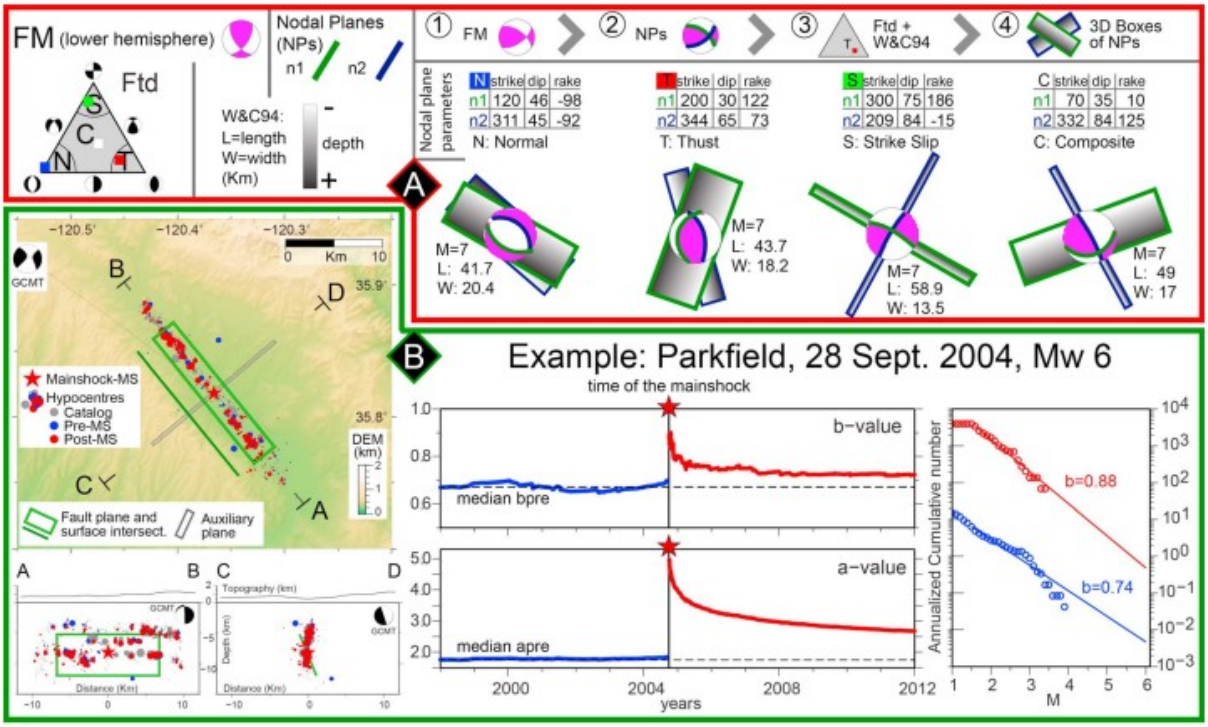

Figure 1

Top panel—red frame: Schematic workflow: from the FM to the fault planes and an example of the inferred geometry for a *M*7 earthquake in different tectonic styles. Top panel (A)—red frame: method details about the four steps to constrain the geometry of the box: from FM (n.1; lower hemisphere, in violet) to nodal planes (NPs in green and blue colors, n.2). By plotting the nodal planes parameters (strike, dip, and rake) in a Frohlich (1992) triangular diagram (Ftd, n.3), we deduce the tectonic style (N = normal, T = thrust, S = strike slip, C = composite) and we infer the plane dimensions (length: L and width: W) as function of the magnitude (*M*) and of the empirical formulas of Wells and Coppersmith (Wells & Coppersmith, 1994). The geometry of the nodal planes (dip direction in shades of gray) and their dimensions constrain the seismogenic boxes (n.4). Four examples for FMs with *M* = 7 and different tectonic styles are reported to display the planes that individuate the fault plane and the

auxiliary one. Bottom panel (B)—green frame. On the left (map): seismicity data plot on a local high resolution Digital Elevation Model (DEM): mainshock (red star), earthquakes below the magnitude of completeness (gray), background (blue), and aftershocks (red). The fault plane (green) is also represented in longitudinal (A-B) and transversal (C-D) sections with respect to the strike. On the right, an example: *a* value and *b* value time series and FMD for the background (blue) and the first *b* value estimated after the mainshock (red) for the M6 Parkfield quake in 2004. FMD = frequency magnitude distribution; FM = focal mechanism.

We processed all magnitude 6.0 or larger independent (i.e., not themselves aftershocks, according to Gardner & Knopoff, 1974), events available to us in the high-quality catalogs (i.e., local catalogs with a low magnitude of completeness) covering California (ANSS), Japan (JMA), Italy (Gasperini et al., 2013), and Alaska (AEIC), giving us 58 sequences in all: 20 in California, 35 in Japan, 2 in Italy, and 1 in Alaska. For each of these mainshocks, we construct a box based on the FM parameters (Figure 1). In order to quickly and homogeneously compare worldwide sequences, all the boxes were derived using mechanisms from the Global Centroid Moment Tensor database (Dziewonski et al., 1981; Ekström et al., 2012), whereas we performed the temporal parameter analysis based on the local catalogs, taking advantage of lower completeness magnitudes and higher location accuracy. Although the Global Centroid Moment Tensor also provides coordinates of the FM centroid, we placed the box at the hypocenter listed in the corresponding local catalog. Sometimes, the offset between those two locations can be significant (tens of kilometers) because centroids are poorly constrained by the Moment Tensor inversion procedure (Kagan, 2003; Smith & Ekström, 1997) and are thus unreliable in many cases. This choice can result in asymmetric distributions of the events with respect to their hypocenter for sources with strong directivity and asymmetric fault rupture. To acknowledge variation in the spatial spread of aftershocks between different sequences, we estimate the density of events (immediate aftershocks, e.g., during the first days) calculating the ratio between the number of events at increasing distances from the box—from 3 to 10 km, in all the 3-D directions—and the fault length. We then choose the distance that yields the highest aftershock density (i.e., the highest ratio). The 3 and 10 km represent, respectively, the uncertainty in the fault size estimation for a *M*6 and for a *M*7 due to the magnitude conversion and homogenization process (e.g., in the Italian catalog; Gasperini et al., 2013). Within this distance from the box, we select all events in the local catalog.

2.1 The Individual Time Series

To compute parameters, we choose a constant number of events approach, moving the window through the catalog event by event and plotting the data at the end of the considered time interval (Tormann et al., 2013). Computing the *b* values critically depends on the correct estimate of the magnitude of completeness (Mc; Mignan & Woessner, 2012; Wiemer & Wyss, 2000; Woessner & Wiemer, 2005) which is known to vary over time and changes especially strongly after large earthquakes (Wiemer & Katsumata, 1999). To avoid overly conservative estimates at times when smaller events were

recorded properly, we estimate the Mc for each time interval and apply a four-level approach: we first estimate the overall completeness based on the maximum curvature method (Wiemer & Wyss, 2000) of the premainshock catalog as well as the second half of the Gardner and Knopoff (1974) aftershock time window (when incompleteness that affects the first phase of the aftershock process is not considered problematic any more), assuming this to be the best Mc level for this region, and use the maximum of those two as the precutting level. We then estimate for each time window Mc via maximum curvature plus 0.2 (Wiemer & Wyss, 2000; Woessner & Wiemer, 2005) to reach the data set from which we estimate the *a* and *b* values if more than 50 events, above the Mc, are available.

To account in addition for the short-term aftershock incompleteness (Kagan, 2004), we removed any events that occurred after the mainshock until the Mc calculated by using the mainshock magnitude-dependent Mc estimate proposed by Helmstetter et al. (2006) matched the precutting level.

We adopt a window length of 150 for the events preceding the mainshock and 400 for events following the mainshock, due to their different abundances. The *b* value was calculated using the maximum likelihood method. For most earthquake sequences, numerous aftershocks are observed within the box, but there is only very sparse background seismicity before the mainshock, too little to estimate an event specific *b* value. In those cases, we estimate a regional background *b* value, selecting the closest 300 events that occurred before the mainshock and using this data set to compute the local reference *b*value. In such cases, the *b* values preceding the mainshocks are not represented by a time series but by a single point preceding the mainshock.

To assess the linearity of each FMD, we adopt the nonlinearity index (NLI; Tormann et al., 2014): this algorithm judges the linearity of a sample catalog based on the *b* value estimates for different cutoff magnitudes, starting at Mc and increasing up to the highest magnitude above which 50 events are still observed. The NLI index is the ratio of the standard deviation of these *b* value estimates divided by the largest individual uncertainty (Shi & Bolt, 1982) in the single *b* value estimates, if at least five *b* value estimates can be calculated. If NLI > = 1, the FMD is considered linear. The overall approach is summarized in Figure 1 for the example of the *M*6. Parkfield (California) mainshock that occurred on 28 September 2004: the time series of *a* values reveals an increase in aftershock activity of roughly a factor of 1,000, which decreases exponentially over time. The *b* values increase by about 20%, from about 0.74 to 0.88, then gradually decrease over time. The respective FMDs are shown, too. In total, we can define the parameters of interest for 31 sequences out of 58 (15 in California, 14 in Japan, 1 in Italy, and 1 in Alaska).

Once the individual time series has been estimated, we normalize it by taking the median value of all the premainshock estimates. Then, for each

time step (i.e., 1 day), we calculate the percentage differences from the reference level (100%). This allows us to stack the individual time series even though the absolute *b* values vary due to different tectonic regimes, magnitude scales, and other factors. Since we are interested in solving potential systematic changes in the parameters before and after the mainshock, we also shifted the time of the mainshock to zero for each sequence and interpolated the derived parameters on a daily scale for the sequence-specific catalog length before and after the mainshock. Finally, we stacked all the 31 sequences: for each day we calculate the mean of the estimates for the individual sequences to derive the general behavior. We establish the uncertainty around the mean by a bootstrap technique over a paradata set of 10 times the number of sequences (i.e., 310).

3 Results

In Figures 2a–2d, we show the results of the time-shifted, normalized, stacked time series, revealing a trend: immediately after the mainshock, the *b* value increases by about 20% (Figure 2a), a jump that is statistically significant and lies outside the observed premainshock variability of the stacked time series. The peak increase in the *b* value occurs at between 1 and 2 months. The *b* value subsequently remains high for the next 5 years, decreasing only gradually. Note also the 10% decrease in *b* value during the months to days prior to the mainshock. While this anomaly is consistent with selected case studies and laboratory studies that have reported dropping precursory *b* values (Gulia et al., 2016; Papadopoulos et al., 2010; Tormann et al., 2015), the number of premainshock stacked time series is only 8.

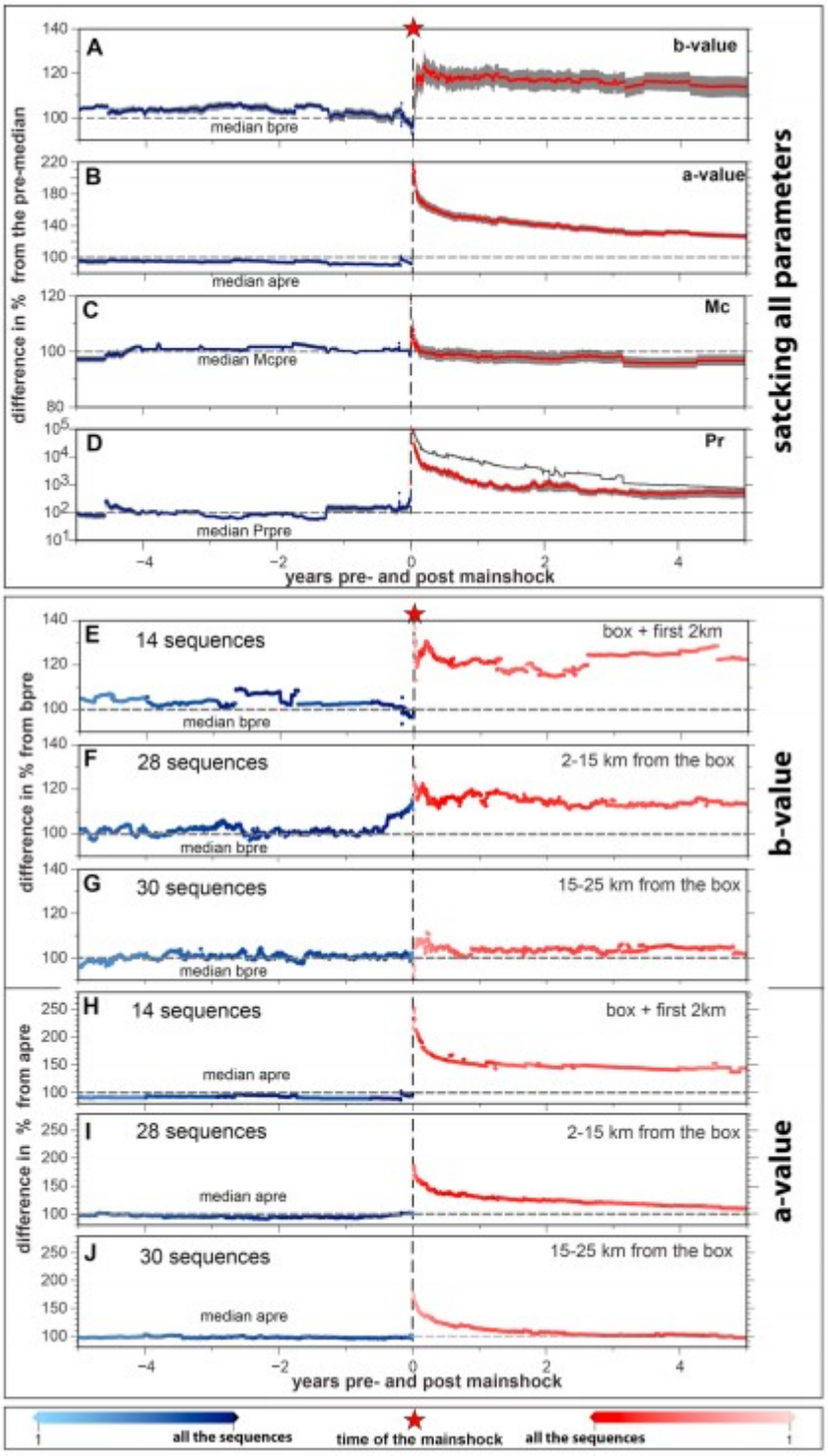

Figure 2

Stacking the parameters of interest for the 31 sequences showing the difference in percentage to the reference value. Blue curves indicate daily values over the 5 years preceding the mainshock. Red curves chart the same values over the first subsequent 5-year period. (a) *b* value. (b) *a* value. (c) Magnitude of completeness. (d) Daily probability for an event with magnitude greater or equal to the mainshock, calculated from the values in the subplots a and b (Pr). In black, the same probability estimated using the background constant *b* value. Gray indicates the uncertainty by bootstrap.

Stacking *b* values (e–g) and *a* values (h–j) as a function of the distance, resampling the subcatalog and estimating *a* and *b* values for the events inside three different volumes. The shaded colors (red and blue) represent the number of sequences that have an estimation.

The stack of the *a* value (Figure 2b) exhibits the well-known increase in activity by a factor of 1,000 after a mainshock, followed by exponential decay. We also show the Mc stack over time (Figure 2c) that indicates no systematic change in the Mc before and after the mainshock. The instantaneous *a* and *b* values can be used to directly compute the probability of an earthquake of any magnitude (Gulia et al., 2016; Wiemer & Wyss, 1997). Of special interest is the probability of a secondary event equal to or even larger than the mainshock itself. The curve of this normalized probability is plotted in Figure 2d. It shows an increase above the premainshock background level by a factor of 10,000 immediately after the mainshock and then a gradual decrease. For comparison, we also compute the current best practice in aftershock hazard assessment, using a constant *b* value (black line in Figure 2d): this probability exceeds the one computed with a temporally varying *b* value by a factor of at least 10 for many years.

Next, we analyze the spatial extent of the *b* value increase by stacking three different and independent sampling volumes around the mainshock fault volume (Figures 3e–3j): the highest increase in both *b* and *a* values is observed in the volume limited to up to 2 km away from the mainshock. Here the *b* values increase by 30% after the mainshock. Volumes between 2 and 15 km away from the mainshock also have higher *b* values, up by about 20% and provide an enticing hint that *b* values in this distance range tend to increase during the months prior to the mainshock, a trend opposite to the precursory decrease observed in the immediate vicinity of the quake. In volumes from 15 to 25 km away, the *b* values increase by only about 5% after the mainshock, while *a* values rise much more sharply, indicating that not only the temporal recovery but also the two spatial footprint changes appear to be different.

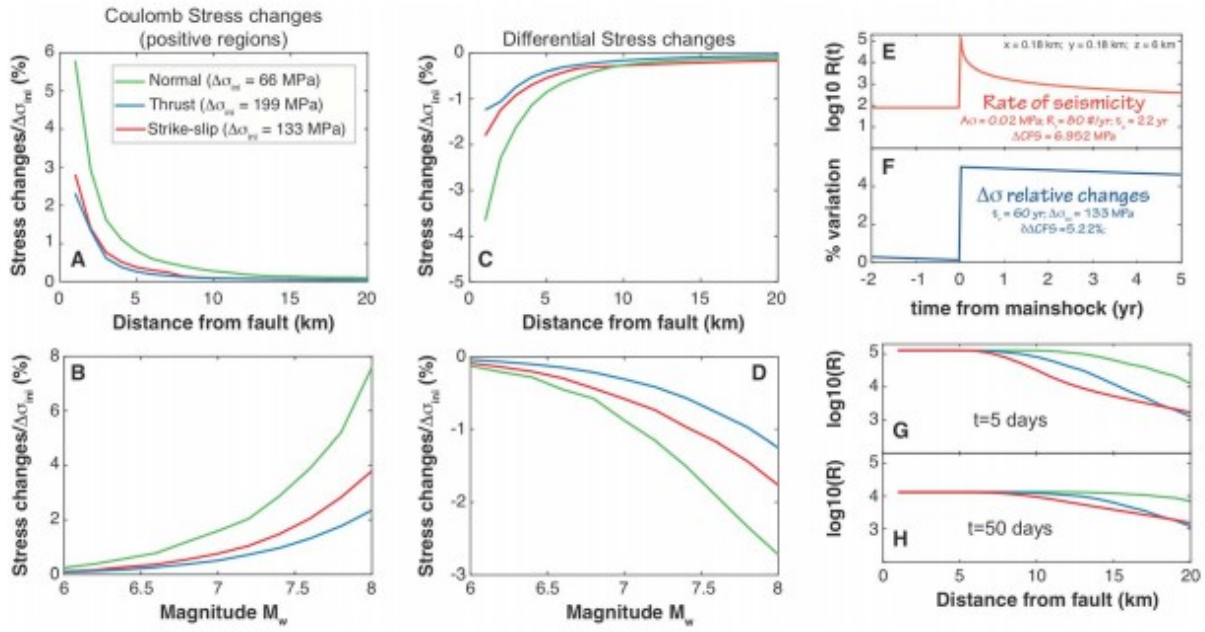

Figure 3

Percentage variation of positive Coulomb Failure Stress changes as function of distance (a) and magnitude (b) for the three different styles of faulting. Percentage variation of differential stress changes as function of distance (c) and magnitude (d). Expected temporal evolution of the seismicity rates (e) and of stress changes recovery (f). Earthquake productivity as function of distance for 5 days (g) and 50 days (h) after mainshock for three different styles of faulting.

4 Modeling the Changes in Aftershocks Distribution

The occurrence of an earthquake affects the stress distribution in the area surrounding the fault zone. For each point of a 3-D domain, the stress changes caused by a mainshock can be computed using analytical solutions for a dislocation in an elastic half-space (Okada, 1992). Such computation provides the full stress tensor at each evaluation point, making it then straightforward to derive variables such as the differential stress changes and the Coulomb Failure Stress (CFS).

On the one hand, the variation in differential stress can be computed assuming an initial state (dependent on the faulting style and resulting in a $\Delta\sigma_{ini} = \sigma_1 - \sigma_3$) and recalculating the principal stress by solving for the eigenvalues in the final configuration (i.e., after summing the changes computed by the Okada model). Then, the differential stress change in percentage is

$$\delta\Delta\sigma = (\Delta\sigma_{fin} - \Delta\sigma_{ini})/\Delta\sigma_{ini}$$

The values of the initial principal stresses are chosen such that $\Delta\sigma_{ini}$ is 66, 133, 199 MPa for normal, strike-slip, and thrust faulting, respectively. These values are calculated assuming that one of the three principle stresses is always the lithostatic and vertical at a seismogenic depth of 9 km with rock density 2,500 kg/m^3. The maximum and minimum principal stresses to calculate the differential stress for the respective cases (normal, strike slip,

and thrust) are then calculated using ratio with respect to the vertical stress. On the other hand, computing changes in CFS provides a first-order understanding of where future aftershocks are likely to occur (Stein, 1999). We can calculate a scaled changes in CFS as

$$\delta\ \Delta\mathrm{CFS} = (\Delta\tau + \mu(\Delta\sigma_n + B\sigma_m))/\Delta\sigma_{\mathrm{Ini}}$$

in which $\Delta\tau$ is shear stress and $\Delta\sigma_n$ is the normal stress. μ is the frictional coefficient with a value of 0.6, with σ_m being the mean effective stress and B = 0.5 the Skempton's coefficient. We consider an elastic medium with a Young's modulus of 30 GPa and a Poisson's ratio of 0.3. The calculated variations for both stress and CFS are dependent on the assumed FM, and we assume that both source and receivers have the same orientation, with a strike of roughly 30° and a dip of 90° for the strike-slip faults and fault dipping ~60° for normal faults and ~30° for thrusts, with both cases having strike of 0°. Such angles represent the optimal orientation if the principal stresses are oriented along coordinate axes.

In order to have an understanding of the stress variation in three dimensions, we calculate the mean spatial variation of both $\delta\Delta\sigma$ and $\delta\Delta$CFS for regions at varying distances from the fault in 1-km steps (e.g., the value at 3 km accounts for values at the receiver between 2 and 3 km). To avoid singular values, we always exclude values in the first 0.5 km.

Figures 3a and 3c show an example of the expected variation in space for an optimally oriented fault reactivating in a M_w = 7 mainshock, with dimensions based on empirical relationship (Wells & Coppersmith, 1994) and top of the fault at 7-km depth. The areas near the fault plane are subjected to a decrease in differential stress or an average larger value of CFS, which correlates with the observed increase in b value.

To analyze this effect as a function of magnitude, we take the average value of relative stress changes within the first 5 km. Figures 3b and 3d shows the variation of average CFS and differential stress changes as a function of magnitude, with percentage variation being proportional (inversely proportional) to the average value of positive Coulomb (differential stress). The model predicts a change of about 8% for CFS and 3% for differential stress at a distance of 5 km for the case of normal faults with magnitude M_w = 8.

Figures 3a–3d refer to coseismic variation; we can use a well-established constitutive law for earthquake production and a classical elastic rebound theory for the stress to extrapolate the temporal variation of the changes in the seismicity rate and percentage variation of differential stress.

The temporal evolution of the earthquake productivity is calculated by assuming rate-and-state friction (Dieterich et al., 2000) according to the formula

$$\frac{R}{r} = \left[\left(e^{-\Delta S/A\sigma_{n,0}} - 1\right)e^{-t/t_a} + 1\right]^{-1}$$

where R is the expected rate of aftershocks at time t, r is the background rate of seismicity, t_a is the aftershock decay time A is a constant value, and $\sigma_{n,0}$ is the value of the normal effective stress. ΔS is an equivalent Coulomb stress, defined as

$$\Delta S = \Delta\tau + \left(\frac{\tau_0}{\sigma_{n,0}} - \alpha\right)(\Delta\sigma_n + p)$$

We use an equivalent friction $\mu = \tau_0/\sigma_{n,0} - \alpha = 0.3$, and the value of $A\sigma_{n,0}$ depends on the faulting style (0.0116, 0.0214, and 0.02 MPa, for normal, thrust, and strike slip, respectively—Heimisson & Segall, 2018). The temporal evolution of differential stress is simply calculated by assuming linear elastic rebound theory: coseismic slip is completely recovered with a given recurrence time.

Figures 3e and 3f show the expected temporal evolution for a point located 1 km above the fault zone along dip. The seismicity rate increases up to 10^5 earthquakes/years and decreases exponentially over time to a value slightly above the background level (80 events per year) after 5 years (Figure 3e). If the stress recovery is elastic, and assuming for example an arbitrarily selected 60-years recurrence period, the CFS, for example, recovers linearly with little change over the first 5 years, remaining at about 5% above the regional value (Figure 3f). A similar trend could be extrapolated for the differential stress, although with negative average value in the considered domain. The chosen recurrence period was assumed quite short to illustrate that even in a case of unusually fast recovery, in a 5-year time frame the stresses are still far from the background value (if assuming elastic response only).

Similar to stress change, the spatial distribution and amplitude of earthquake productivity depend on the fault's orientation and faulting style. A comparison of the results in Figures 3g and 3a/3c shows that for the three different faulting styles we expect differences in seismicity and relative stress changes, with normal faults being the most receptive, but the general trends persist. While the rate of aftershocks strongly increased up to 10 km away from the fault (depending on the tectonic style), the stress changes are largely confined to an area within the first 5 km from the fault.

Summing up, our simple model shown in Figure 3 suggests that areas of positive CFS (or average negative differential stress) exist after a mainshock, which would explain the observed increased b value. Assuming that this correlation does exist, the amplitude of the $b$value increase should depend systematically on magnitude and faulting style. According to the model, the b value should recover slower and linearly with time, rather than decaying exponentially, as observed for aftershock rates. The b value increase should be confined to the immediate vicinity of the mainshocks.

Inspired by these model's predictions, we now reexamine our stacking results. We currently lack the resolution power necessary to analyze

quantitatively the spatial correlation of *b*value increase with areas of positive CFS (or negative differential stress), and we also have too limited FM diversity for a meaningful analysis. We first analyze the long-term trend: in Figures 4a and 4b, we extend the stacks to 15 years after a mainshock occurrence and indeed find the recovery in *b* value to be very different from the change in *a* values. The rate increase decays exponentially with time, as expected and in accordance with Omori's law. After 15 years it almost reached the pre-event background level. In contrast, the *b* values remain high through time, decreasing only slightly, in agreement with our theory.

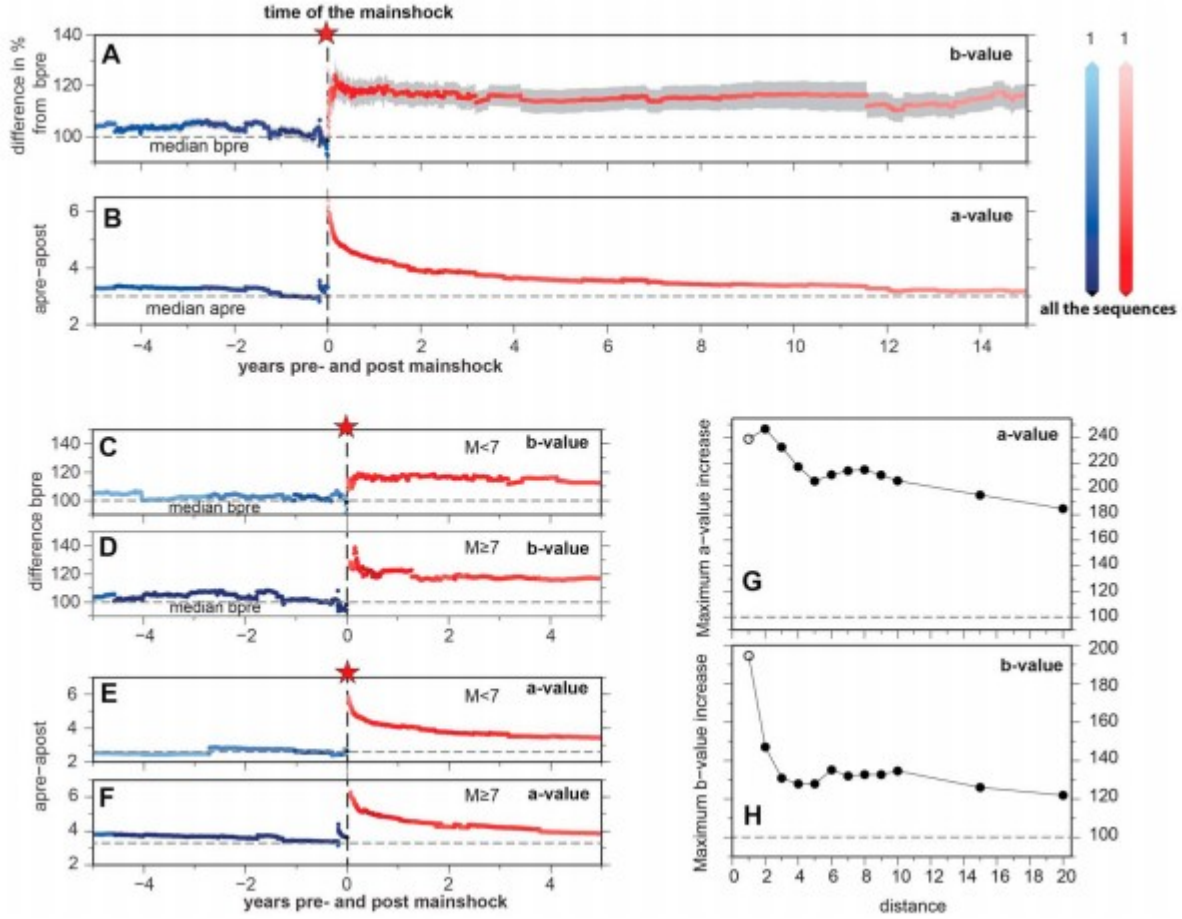

Figure 4

(a, b) *a* value and *b* value stacking showing the difference in percentage from the reference value. (c–f) *b* value stacking and *a* value time series for the 20 sequences with mainshock $M < 7$ and for the 11 sequences with mainshock $M > =7$. Percentage of the maximum *a* value (g) and *b* value (h) increase as a function of the distance from the box (km) over the first 3 months of aftershocks.

To investigate magnitude dependence, we compute stacks of the *b* values for events above and below magnitude 7.0 (Figures 4c and 4d). These confirm that events with magnitude equal or bigger than 7 experience an increase approaching 40%, while smaller mainshocks cause an increase of about 20%. Conversely, the *a* value increase (Figures 4e and 4f) appears rather independent of magnitude. The magnitude dependence of *b* value

increase would be even further pronounced if stress drop depended on magnitude. Although it is often assumed that stress drop is independent of magnitude, for large strike-slip earthquakes it was pointed out that slip increases with rupture length (Scholz, 1982), which has been confirmed more recently (Hanks & Bakun, 2002, 2008). Because these earthquakes all have the same width, constrained by the seismogenic thickness, then stress drop must increase by rupture length and magnitude.

We also study the distance decay kernels in greater detail in Figures 4g and 4h and find that they tally with the theoretical prediction that *b* values increase is confined to the immediate vicinity of the fault, decaying rapidly with distance, whereas *a* value increases decay more gradually with distance from the fault. Our more detailed analysis has therefore shown good agreement between model prediction and data.

5 Discussion and Conclusions

By using stacking of *b* value time series as a tool to enhance the signal-to-noise ratio, our study is the first to quantify the general impact of a mainshock on the size distribution of subsequent earthquakes. The stacked signal of an increase in *b* value by 20–30% after a mainshock is very clear and highly significant (Figure 2). We document for the first time the space, time, faulting style, and magnitude dependency of the *b* values change and establish that the *b* value change transients behave distinctly different from the ones of aftershock rate change, as described in Omori's law. The differential stress change of the mainshock is a highly plausible mechanism explaining the empirical observations and is fully consistent with laboratory measurements of the *b* value dependence on stress.

We propose that the changes in *b* value as a function of time after a mainshock can be described using the formula:

$b_{post} = b_{pre}\ (1 + d\ (1 - t/Rt))$where Rt is the return period of the mainshock and d is a constant that may depend on the magnitude of the mainshock, the faulting style, and possible tectonic region. A default value for d, as observed in Figure 2a, would be 0.2. The observed long-lasting increase on the *b* values matches the fault's loading rate.

Our results address one of the open issues regarding Coulomb stress changes and elastic rebound theory by Reid (1911). Elastic rebound theory predicts that after a mainshock, it will take time to recover the strain released in the mainshock, so the subsequent years should be the least hazardous. On the other hand, Coulomb stress change models and operational aftershock forecasting models such as Epidemic-Type Aftershock Sequence (Ogata, 1988, 1998) or STEP (Short-Term Earthquake Probability, Gerstenberger et al., 2005) predict the highest rate of rerupturing on the same fault immediately after the mainshock. These models forecast an unrealistically high chance for a repeat of the mainshock rupture (Figure 2d) and thus substantially overestimate aftershock hazard. So far, operational

earthquake forecasting models have—on a somewhat ad hoc basis—lowered the maximum magnitude or removed this mainshock fault from their computations (Field et al., 2017). Our results suggest that this paradox is resolved when considering the stress changes and their impact on the earthquake size distribution. While numerous small events occur near the mainshock fault, larger ones are far rarer than existing models predict. Indeed, Figure 4h suggests that the *b* values right on the fault plane increase by much more than 120%, consistent with observations from individual sequences showing that the strongest *b* value change occurs near the patches of the largest slip (Tormann et al., 2015).

CFS analysis after significant earthquakes has been frequently conducted after large mainshocks, with hundreds of studies conducted since the groundbreaking work done on the Landers earthquake (King et al., 1994). The performance assessment of these aftershock forecasts has been mixed (Hardebeck et al., 1998; Nandan et al., 2016). Based on our modeling (Figure 3), we postulate that in the future such studies should consider not only the effect of CFS on earthquake rates but also the absolute value of the change in stress and its impact on earthquake size distribution if they are to forecast earthquake hazard accurately.

We conclude by suggesting that stacking carefully selected, time-shifted, and normalized time series of *b* values has proven to be a powerful approach for gaining insights into physical processes. Our analysis has also shown hints of precursory signals that are consistent with preslip on the fault: decreasing *b* values in the immediate vicinity of the fault and increasing ones nearby (Figures 2e and 2f). Future studies covering more events may be able to resolve these important precursory changes using the stacking approach introduced here.

Acknowledgments

Earthquake catalog data for California were obtained from the Advanced National Seismic System (http://www. ncedc.org/anss/catalog-search.html). We thank JMA for sharing the earthquake catalog. Data are available from authors upon request. Figures were produced with the Generic Mapping Tools (http://gmt.soest.hawaii.edu). The authors thank the Editor, Gavin Hayes, Chris Scholz, and one anonymous reviewer for helping in improving and clarifying the manuscript. The authors declare no competing financial interests.

References

Amitrano, D. (2003). Brittle-ductile transition and associated seismicity: Experimental and numerical studies and relationship with the *b* value. *Journal of Geophysical Research*, 108(B1), 2044. https://doi.org/10.1029/2001JB000680

Bachmann, C. E., Wiemer, S., Goertz-Allmann, B. P., & Woessner, J. (2012). Influence of pore-pressure on the event-size distribution of induced

earthquakes. *Geophysical Research Letters*, 39, L09302. https://doi.org/10.1029/2012GL051480

Dieterich, J. H., Cayol, V., & Okubo, P. G. (2000). The use of earthquake rate changes as a stress meter at Kilauea volcano. *Nature*, 408(6811), 457– 460. https://doi.org/10.1038/35044054

Dziewonski, A. M., Chou, T. A., & Woodhouse, J. H. (1981). Determination of earthquake source parameters from waveform data for studies of global and regional seismicity. *Journal of Geophysical Research*, 86, 2825– 2852. https://doi.org/10.1029/JB086iB04p02825

Ebel, J. E., Bonjer, K.-P., & Oncescu, M. C. (2000). Paleoseismicity: Seismicity evidence for past large earthquakes. *Seismological Research Letters*, 71(2), 283– 294. https://doi.org/10.1785/gssrl.71.2.283

Ekström, G., Nettles, M., & Dziewoński, A. M. (2012). The global CMT project 2004–2010: Centroid-moment tensors for 13,017 earthquakes. *Physics of the Earth and Planetary Interiors*, 200–201, 1– 9.

Field, E. H., Jordan, T. H., Page, M. T., Milner, K. R., Shaw, B. E., Dawson, T. E., Biasi, G. P., Parsons, T., Hardebeck, J. L., Michael, A. J., Weldon, R. J. II, Powers, P. M., Johnson, K. M., Zeng, Y., Felzer, K. R., Elst, N. . ., Madden, C., Arrowsmith, R., Werner, M. J., & Thatcher, W. R. (2017). A synoptic view of the third uniform California earthquake rupture forecast (UCERF3). *Seismological Research Letters*, 88(5), 1259– 1267. https://doi.org/10.1785/0220170045

Frohlich, C. (1992). Triangle diagrams: Ternary graphs to display similarity and diversity of earthquake focal mechanisms. *Physics of the Earth and Planetary Interiors*, 75(1-3), 193– 198. https://doi.org/10.1016/0031-9201(92)90130-N

Gardner, J. K., & Knopoff, L. (1974). Is the sequence of earthquake in Southern California, with aftershocks removed. Poissonian? *Bulletin of the Seismological Society of America*, 66, 1271– 1302.

Gasperini, P., Lolli, B., & Vannucci, G. (2013). Empirical calibration of local magnitude data sets versus moment magnitude in Italy. *Bulletin of the Seismological Society of America*, 103(4), 2227– 2246. https://doi.org/10.1785/0120120356

Gerstenberger, M. C., Wiemer, S., Jones, L. M., & Reasenberg, P. A. (2005). Real-time forecasts of tomorrow's earthquakes in California. *Nature*, 435(7040), 328– 331. https://doi.org/10.1038/nature03622

Goebel, T. H. W., Schorlemmer, D., Becker, T. W., Dresen, G., & Sammis, C. G. (2013). Acoustic emissions document stress changes over many seismic cycles in stick-slip experiments. *Geophysical Research Letters*, 40, 2049– 2054. https://doi.org/10.1002/grl.50507

Gulia, L., Tormann, T., Wiemer, S., Herrmann, M., & Seif, S. (2016). Short-term probabilistic earthquake risk assessment considering time-dependent b values. *Geophysical Research Letters*, 43, 1100– 1108. https://doi.org/10.1002/2015GL066686

Gulia, L., & Wiemer, S. (2010). The influence of tectonic regimes on the earthquake size distribution: A case study for Italy. *Geophysical Research Letters*, 37, L10305. https://doi.org/10.1029/2010GL043066

Gutenberg, B., & Richter, C. F. (1944). Frequency of earthquakes in California. *Bulletin of the Seismological Society of America*, 34, 185– 188.

Hanks, T. C., & Bakun, W. H. (2002). A bilinear source-scaling model for M-log A observations of continental earthquakes. *Bulletin of the Seismological Society of America*, 92(5), 1841– 1846. https://doi.org/10.1785/0120010148

Hanks, T. C., & Bakun, W. H. (2008). M-log A observations for recent large earthquakes. *Bulletin of the Seismological Society of America*, 98(1), 490– 494. https://doi.org/10.1785/0120070174

Hardebeck, J. L., Nazareth, J. J., & Hauksson, E. (1998). The static stress change triggering model: Constraints from two southern California aftershock sequences. *Journal of Geophysical Research*, 103, 24,427– 24,437. https://doi.org/10.1029/98JB00573

Heimisson, E. R., & Segall, P. (2018). Constitutive law for earthquake production based on rate-and-state friction: Dieterich 1994 revisited. *Journal of Geophysical Research: Solid Earth*, 123, 4141– 4156. https://doi.org/10.1029/2018JB015656

Helmstetter, A., Kagan, Y. Y., & Jackson, D. D. (2006). Comparison of short-term and time-independent earthquake forecast models for Southern California. *Bulletin of the Seismological Society of America*, 96(1), 90– 106. https://doi.org/10.1785/0120050067

Kagan, Y. Y. (2003). Accuracy of modern global earthquake catalogs. *Physics of the Earth and Planetary Interiors*, 135(2-3), 173– 209. https://doi.org/10.1016/S0031-9201(02)00214-5

Kagan, Y. Y. (2004). Short-term properties of earthquake catalogs and models of earthquake source. *Bulletin of the Seismological Society of America*, 94(4), 1207– 1228. https://doi.org/10.1785/012003098

King, G. C. P., Stein, R. S., & Lin, J. (1994). Static stress changes and the triggering of earthquakes. *Bulletin of the Seismological Society of America*, 84(3), 935– 953.

Marzocchi, W., Taroni, M., & Falcone, G. (2017). Earthquake forecasting during the complex Amatrice-Norcia seismic sequence. *Science Advances*, 3(9), e1701239. https://doi.org/10.1126/sciadv.1701239

Mignan, A. (2015). Modeling aftershocks as a stretched exponential relaxation. *Geophysical Research Letters*, 42, 9726– 9732. https://doi.org/10.1002/2015GL066232

Mignan, A. (2016). Reply to ‘comment on “revisiting the 1894 Omori aftershock dataset with the stretched exponential function” by A. Mignan’ by S. Hainzl & A. Christophersen. *Seismological Research Letters*, 87, 1134–1137.

Mignan, A., & Woessner, J. (2012). Estimating the magnitude of completeness for earthquake catalogs. *Community Online Resource for Statistical Seismicity Analysis*. https://doi.org/10.5078/corssa-00180805

Nandan, S., Ouillon, G., Woessner, J., Sornette, D., & Wiemer, S. (2016). Systematic assessment of the static stress triggering hypothesis using interearthquake time statistics. *Journal of Geophysical Research: Solid Earth*, 121, 1890– 1909. https://doi.org/10.1002/2015JB012212

Ogata, Y. (1988). Statistical models for earthquake occurrences and residual analysis for point processes. *Journal of the American Statistical Association*, 83(401), 9– 27. https://doi.org/10.1080/01621459.1988.10478560

Ogata, Y. (1998). Space-time point-process models for earthquake occurrences. *Annals of the Institute of Statistical Mathematics*, 50(2), 379–402. https://doi.org/10.1023/A:1003403601725

Ogata, Y., & Katsura, K. (2014). Comparing foreshock characteristics and foreshock forecasting in observed and simulated earthquake catalogs. *Journal of Geophysical Research: Solid Earth*, 119, 8457– 8477. https://doi.org/10.1002/2014JB011250

Okada, Y. (1992). Internal deformation due to shear and tensile faults in a half-space. *Bulletin of the Seismological Society of America*, 82, 1018– 1040.

Omori, F. (1895). On the aftershocks of earthquakes. *Journal of the College of Science, Imperial University of Tokyo*, 7, 111– 200.

Papadopoulos, G. A., Charalampakis, M., Fokaefs, A., & Minadakis, G. (2010). Strong foreshock signal preceding the L'Aquila (Italy) earthquake (Mw 6.3) of 6 April 2009. *Natural Hazards and Earth System Sciences*, 10(1), 19– 24. https://doi.org/10.5194/nhess-10-19-2010

Reid, H. F. (1911). The elastic-rebound theory of earthquakes. *Bulletin of the Department of Geology of the University of California*, 6, 413– 444.

Scholz, C. H. (1968). The frequency-magnitude relation of microfracturing in rock and its relation to earthquakes. *Bulletin of the Seismological Society of America*, 58, 399– 415.

Scholz, C. H. (1982). Scaling laws for large earthquakes: Consequences for physical models. *Bulletin of the Seismological Society of America*, 72, 1– 14.

Schorlemmer, D., Wiemer, S., & Wyss, M. (2005). Variations in earthquake-size distribution across different stress regimes. *Nature*, 437(7058), 539– 542. https://doi.org/10.1038/nature04094

Shi, Y., & Bolt, B. (1982). The standard error of the magnitude-frequency b value. *Bulletin of the Seismological Society of America*, 72, 1677– 1687.

Smith, G. P., & Ekström, G. (1997). Interpretation of earthquake epicenter and CMT centroid locations, in terms of rupture length and direction. *Physics of the Earth and Planetary Interiors*, 102(1-2), 123– 132. https://doi.org/10.1016/S0031-9201(96)03246-3

Spada, M., Tormann, T., Wiemer, S., & Enescu, B. (2013). Generic dependence of the frequency-size distribution of earthquakes on depth and its relation to the strength profile of the crust. *Geophysical Research Letters*, 40, 709– 714. https://doi.org/10.1029/2012GL054198

Stein, R. S. (1999). The role of stress transfer in earthquake occurrence. *Nature*, 402(6762), 605– 609. https://doi.org/10.1038/45144

Tamaribuchi, K., Yagi, Y., Enescu, B., & Hirano, S. (2018). Characteristics of foreshock activity inferred from the JMA earthquake catalog. *Earth, Planets and Space*, 70(1), 90. https://doi.org/10.1186/s40623-018-0866-9

Toda, S., Stein, R. S., Richards-Dinger, K., & Bozkurt, S. B. (2005). Forecasting the evolution of seismicity in southern California: Animations built on earthquake stress transfer. *Journal of Geophysical Research*, 110, B05S16. https://doi.org/10.1029/2004JB003415

Tormann, T., Enescu, B., Woessner, J., & Wiemer, S. (2015). Randomness of megathrust earthquakes implied by rapid stress recovery after the Japan earthquake. *Nature Geoscience*, 8(2), 152– 158. https://doi.org/10.1038/ngeo2343

Tormann, T., Wiemer, S., & Hardebeck, J. L. (2012). Earthquake recurrence models fail when earthquakes fail to reset the stress field. *Geophysical Research Letters*, 39, L18310. https://doi.org/10.1029/2012GL052913

Tormann, T., Wiemer, S., Metzger, S., Michael, A., & Hardebeck, J. L. (2013). Size distribution of parkfield's microearthquakes reflects changes in surface creep rate. *Geophysical Journal International*, 193(3), 1474– 1478. https://doi.org/10.1093/gji/ggt093

Tormann, T., Wiemer, S., & Mignan, A. (2014). Systematic survey of high-resolution b value imaging along Californian faults: Inference on asperities. *Journal of Geophysical Research: Solid Earth*, 119, 2029– 2054. https://doi.org/10.1002/2013JB010867

Utsu, T. (1961). A statistical study on the occurrence of aftershocks. *Geophysical Magazine*, 30, 521– 605.

Utsu, T., Ogata, Y., Ritsuko, S., & Matsu'ura (1995). The centenary of the Omori formula for a decay law of aftershock activity. *Journal of Physics of the Earth*, 43, 1– 33.

Wells, D. L., & Coppersmith, K. J. (1994). New empirical relationships among magnitude, rupture length, rupture width, rupture area, and surface displacement. *Bulletin of the Seismological Society of America*, 84, 974–1002.

Wiemer, S., Gerstenberger, M., & Hauksson, E. (2002). Properties of the aftershock sequence of the 1999 Mw 7.1 Hector Mine earthquake: Implications for aftershock hazard. *Bulletin of the Seismological Society of America*, 92(4), 1227– 1240. https://doi.org/10.1785/0120000914

Wiemer, S., & Katsumata, K. (1999). Spatial variability of seismicity parameters in aftershock zones. *Journal of Geophysical Research*, 104, 13,135– 13,151. https://doi.org/10.1029/1999JB900032

Wiemer, S., & Wyss, M. (1997). Mapping the frequency-magnitude distribution in asperities: An improved technique to calculate recurrence times? *Journal of Geophysical Research*, 102, 15,115– 15,128. https://doi.org/10.1029/97JB00726

Wiemer, S., & Wyss, M. (2000). Minimum magnitude of completeness in earthquake catalogs: Examples from Alaska, the Western United States, and Japan. *Bulletin of the Seismological Society of America*, 90(4), 859– 869. https://doi.org/10.1785/0119990114

Wiemer, S., & Wyss, M. (2002). Mapping spatial variability of the frequency-magnitude distribution of earthquakes. *Advances in Geophysics*, 45, 259–302. https://doi.org/10.1016/S0065-2687(02)80007-3

Woessner, J., & Wiemer, S. (2005). Assessing the quality of earthquake catalogs: Estimating the magnitude of completeness and its uncertainty. *Bulletin of the Seismological Society of America*, 95(2), 684– 698. https://doi.org/10.1785/0120040007

Wyss, M., & Wiemer, S. (2000). Change in the probability for earthquakes in southern California due to the Landers magnitude 73 earthquake. *Science*, 290(5495), 1334– 1338.